Transactions of JWRI, Vol. 37 (2008), No. 1

Numerical and Experimental Investigations on Welding Deformation†

WANG Rui *, RASHED Sherif **, SERIZAWA Hisashi*, MURAKAWA Hidekazu**** and Jianxun ZHANG *******

Abstract

Prediction of welding distortion of different materials and welding joints in reasonable time is essential in the welding industry. In this paper, a three dimensional thermo-elastic-plastic finite element method (FEM) using an in-house finite element code of iterative substructure method (ISM) is developed to precisely predict welding distortion in bead on plate welding and fillet welding with SUS304 stainless steel and SS400 carbon steel. In addition, the corresponding experiments are carried out to validate the predicted results. Research results show the predicted results by ISM match the experimental results very well. In the condition of different welding heat inputs, the welding heat input plays an important role in welding distortion. Material properties of stainless steel and carbon steel play a larger role in welding distortion when welding heat input is the same. Further, for bead on plate welding of thin plate, both large distortion theory and small distortion theory are computed. The results show that using large distortion theory is more accurate in predicting welding distortion in thin plate welding.

KEY WORDS: (FEM) (Material property) (Welding distortion) (Bead on plate welding) (Fillet welding) (Large distortion theory)

1. Introduction

During welding processes, the non-uniform expansion and contraction of the weld joint and the surrounding base metal result in mismatched thermal strains, leading to welding residual stresses and permanent distortion. Welding distortion can cause loss of dimensional control and structural integrity and increase fabrication costs. Therefore, simple and adaptable methodologies for predicting welding distortion are desirable.

A number of researchers, theoretically or experimentally have tried to predict the thermal and mechanical responses of welding structure for finding ways to predict welding residual stress and distortion in practice industrial production. Mechaleris et al. [1, 2] combine two-dimensional non-linear transient welding simulations with three-dimensional structural analyses in a decoupled approach. Using two-dimensional thermo-mechanical welding process simulations for determining the temperature loading for a three-dimensional structural model determine buckling distortion after welding in large and complex structures. Gamilleri et al. [3] studied a simplified finite element method to simulate the out-of-plane distortion caused by fusion butt welding. The simplification including deals with the thermal transient process to a simple two-dimensional treatment and the thermo-elastic-plastic process is replaced by simple analytical algorithms. Based on this method, accurate computational results can be obtained within reasonable computational time. Tsai et al. [4] have studied welding distortion and residual stress of a thin plate panel structure using FEA based on the inherent shrinkage method. The effects of welding sequence on distortion, local plate bending and buckling are also discussed. Murakawa et al. [5, 6] studied a highly efficient FE simulation of iterative substructure method for large welding structures in industrial application. Liang et al. [7, 8] studied the inherent distortion distribution in typical welded joints and using inherent strain methods to predict the welding distortion for large structures. Deng et al. [9~ 11] used FEM combined with experimental research to precisely predict the welding distortion. The large distortion theory was also discussed to predict welding residual and distortion for 1mm thickness plate. McDill et al. [12] discussed the effect of material properties on welding distortion in carbon and stainless steels. They concluded that thermal properties play a larger role in distortion.

In this study, a high speed and high accuracy FE program of interactive substructure method (ISM) is proposed to estimate the welding distortion of SUS304 stainless steel and SS400 carbon steel in different

† Received on July 11, 2008
* Foreign Visiting Researcher, Xi'an Jiaotong University
** Specially Appointed Professor
*** Associate professor
*** * Professor
***** Professor, Xi'an Jiaotong University
Transactions of JWRI is published by Joining and Welding Research Institute, Osaka University, Ibaraki, Osaka 567-0047, Japan

welding joints. Using the ISM analysis, welding distortions are simulated in practical computation time. The effects of welding heat input and materials properties on welding distortion of SUS304 stainless steel and SS400 carbon steel are discussed. Meanwhile, a three-dimensional thermal-elastic-plastic finite element simulation based both on the large distortion theory and small distortion theory is used to predict the welding distortion of thin plate. Experiments are also carried out to verify and compare the simulated results.

2. Experimental procedures

Experiments were conducted to collect the welding information. Two typical welding joints, namely bead on plate welding joint and fillet welding joint are discussed in this section. The experimental materials are made of SUS304 stainless steel and SS400 carbon steel. The welding method is CO_2 gas metal arc welding, and the filler materials are GFW308L and MGS-50, respectively. Experimental results were used to verify the finite element model. The experiments were carried out to realize the following functions:

(1) to measure temperatures continuously during welding and cooling, using thermocouples in fixed locations on the specimens.

(2) to measure the macrosection shapes of welding joints.

(3) to measure welding distortions including, transverse shrinkage, angular distortion and longitudinal shrinkage.

2.1 Welding processing

For bead on plate welding, the experimental set up and fixing conditions are shown in **Fig.1** and **Fig.2**, respectively. The plate sizes are 200mm×200mm.The welding conditions are given in **Table 1**.

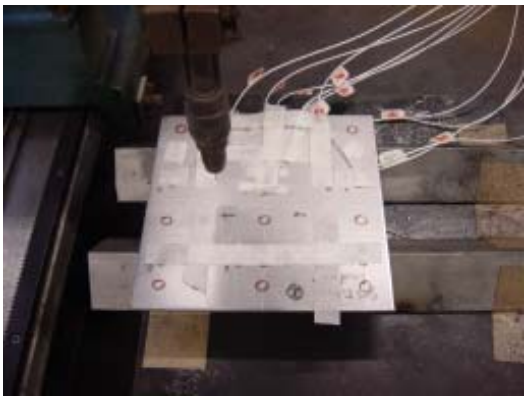

Fig.1 Experimental set up of bead on plate welding

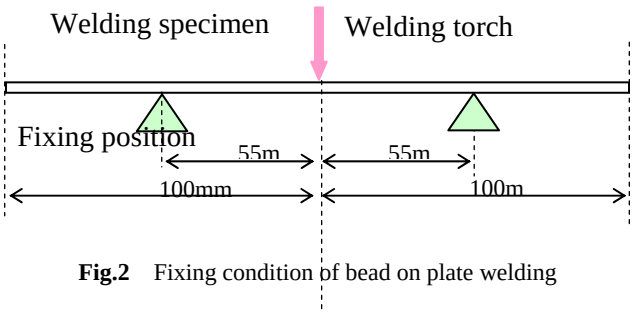

Fig.2 Fixing condition of bead on plate welding

Table 1 Welding condition of bead on plate welding

Case No.	Material	Plate thickness (mm)	Current (A)	Voltage (V)	Speed (cm/min)	Wire feed rate (mm/s)
1	SS400	3.2	140	24.5	50	53
2	SS400	4.5	155	24	40	60
3	SUS304	3.0	80	27	80	53
4	SUS304	5.0	120	28	90	80

For fillet welding, the sizes of the flanges are 200mm×200mm and those of the web are 200mm×50mm. **Fig.3** shows the experimental set up. The fixing condition for fillet welding is same as for bead on plate welding as shown in **Fig.2**. As for the welding sequence, the right-hand joint is welded first. After completely cooling to room temperature, the left-hand joint is welded. The welding parameters are shown in **Table 2**.

Table 2 Welding condition of fillet welding

Case No.	Material	Pass	Plate thickness (mm)	Current (A)	Voltage (V)	Speed (cm/min)	Wire feed rate (mm/s)
5	SS400	1	6.0(flange)-4.5(web)	180	24	30	69
	SS400	2	6.0(flange)-4.5(web)	175	24	30	69
6	SUS304	1	6.0(flange)-5.0(web)	140	28.5	35	88
	SUS304	2	6.0(flange)-5.0(web)	135	28.5	35	87

Fig.3 Experimental set up of fillet welding

2.2 Measurement of temperature

In order to validate the thermal analysis results of FEA, the thermal cycle curves of two joints were measured. The temperature data for each thermocouple were collected during welding. The amount of time is sufficient for the entire plate, in all cases, to cool to a stable temperature. The distributions of measurement points for thermal cycles are shown in **Fig.4**.

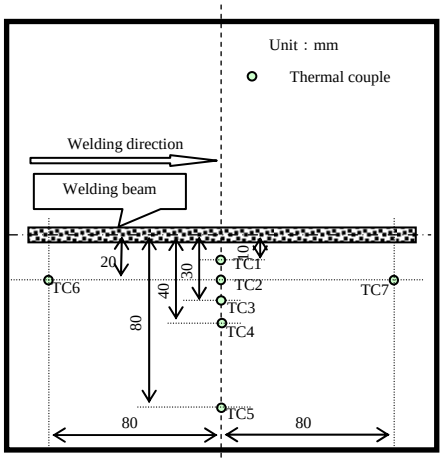

(a) Bead on plate welding

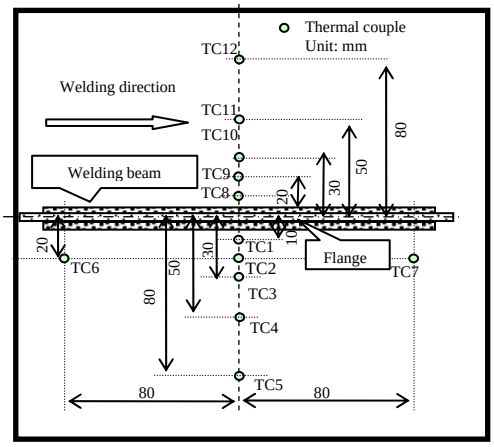

(b) Fillet welding

Fig.4 Distributions of temperature measurement points

2.3 Measurement of welding distortion

In the experiments, welding distortions including, transverse shrinkage, longitudinal shrinkage, and angular distortion were measured on the surface and bottom of the specimens. The distributions of measurement points for each distortion are shown in **Fig.5**, **Fig.6**, and **Fig.7**, respectively. The welding distortion of each measurement point is calculated through the measurement results before and after welding.

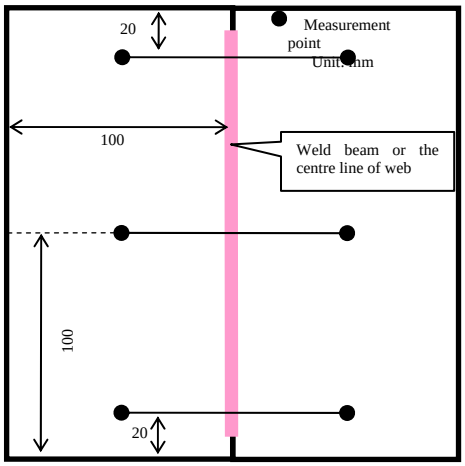

Fig.5 Distributions of transverse shrinkage measurement points

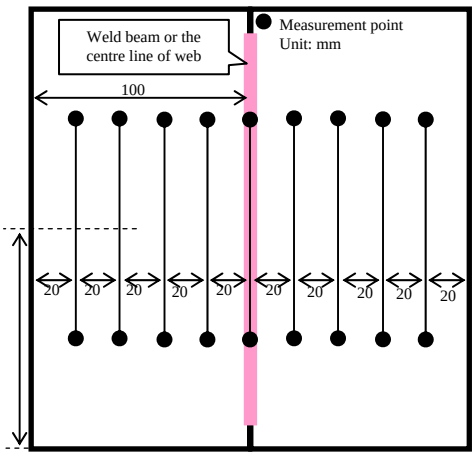

Fig.6 Distributions of longitudinal shrinkage measurement points

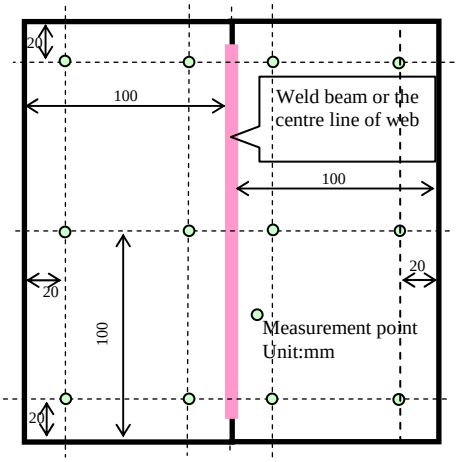

Fig.7 Distributions of angular distortion measurement points

2.4 Measurement macrosection of welding joints

Once all experiments were complete, several samples underwent destructive metallurgical evaluation in order to document the characteristics of weld joints. This evaluation included measurement the macrosection at the midpoint of the weld bead. The macrosection were mounted and measured for overall sizes of weld bead. Experiment results are used to determine dimensional values of joint shapes for computational models. Furthermore, these results can be used to validate the results of thermal analysis.

3 Finite element implementation

Analysis of the complete thermo-mechanical response due to welding will require a full three-dimensional inelastic analysis of thermal and mechanical behavior. In this presentation, the time-independent three-dimensional uncoupled thermal-mechanical analysis is used. Temperature dependent material properties are incorporated in the analysis. For thermal analysis, it is assumed that the energy from the arc to the weldment is applied on the heating area of specimen. The welding conditions used in the experiment determine the magnitude of heat input to the work piece. The parameters of the fusion zone are adjusted according to experimental results. For mechanical analysis, a thermal-elastic-plastic FE procedure based on ISM [6, 13, 14] is developed to calculate welding distortion. ISM takes advantage of the fact that the strong nonlinearity region is limited in a very small area and the remaining part of the model is mostly linear. This method notably reduces the computation time. In order to capture the nonlinear geometrical behavior in the thin plates, the large distortion theory is incorporated into thermo-elastic-plastic FEM in bead on plate welding. The accuracy of the prediction is examined by comparison with experimental results.

3.1 FE model

Fig.8 shows the finite element mesh models, including boundary conditions of bead on plate welding and fillet welding which were used in the simulation. An eight node brick element is used to model the structures. For the bead on plate model, there are 50 and 4 elements in the X and Z direction. In the Y direction, element meshes are denser near the weld centerline and the meshes become gradually coarser away from the weld centerline. This results in 9046 nodes and 6968 elements. For the fillet welding model, the mesh method is the same as for bead on plate welding. It contains a total of 18309 nodes and 14400 elements. The dimensions of the finite element model and the boundary conditions (shown in **Fig.8** by arrows on specimens) are the same as those of the experimental specimens.

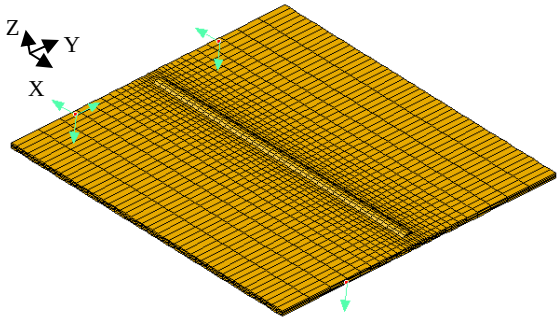

(a) Case 1

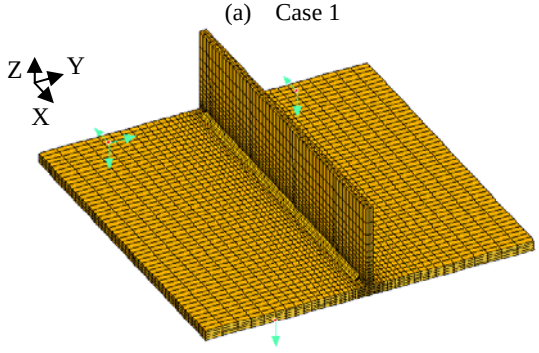

(b) Case 5

Fig.8 Finite element model

3.2 Material model

Welding distortions depend on the geometry, welding condition as well as the material properties. The materials used in this study are SUS304 stainless steel and SS400 carbon steel. An understanding of the role played by material properties on welding distortion of stainless steel and carbon steel will be important. In thermal analysis and mechanical analysis, temperature-dependent thermo-physical and mechanical properties of both SUS304 stainless steel and SS400 carbon steel are considered. The temperature-dependent thermo-physical properties and mechanical properties of the SUS304 and SS400 steels are shown in **Figs.9** and **10**, respectively.

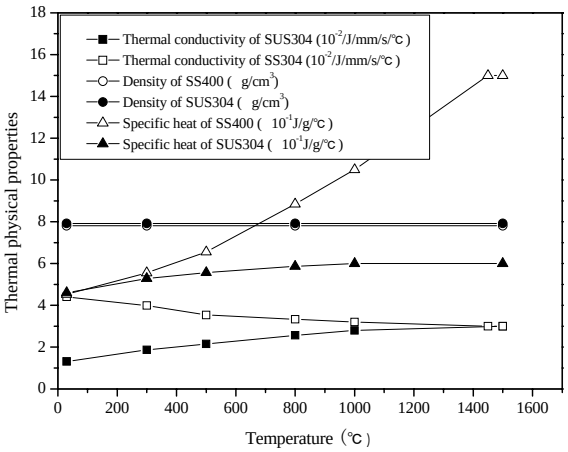

Fig.9 Temperature-dependent thermal physical properties

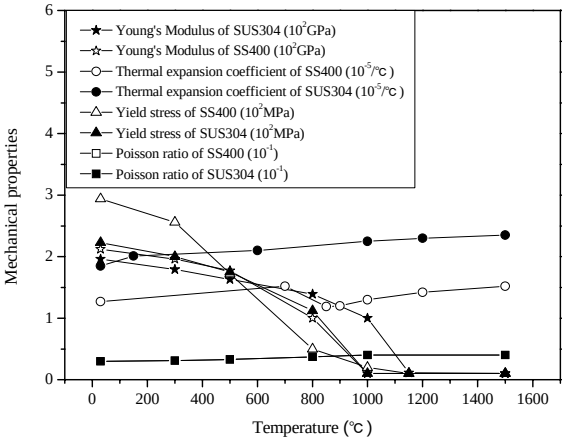

Fig.10 Temperature-dependent thermal mechanical properties

4 Results and discussion

4.1 Welding temperature field

In this section, the computational results of temperature field combined with experimental results are discussed. For bead on plate welding, representative temperatures of five thermocouples (TC 1, TC 2, TC 3, TC 4, and TC5) at the locations shown in **Fig.4 (a)** are picked out. For fillet welding, representative temperatures of three thermocouples (TC 1, TC 2, and TC 3) at the locations shown in **Fig.4 (b)** are discussed.

Fig.11 shows the comparison results between computation and experiment of temperature histories on bead on plate welding. For fillet welding case 5 and case 6, the heat inputs (Q/h2) of these two cases are almost same at 34.35 and 34.07 J/mm3. For the same welding heat input condition, the comparison results between computation and experiment of temperature histories on case 5 and case 6 are shown in **Fig.12 (a)** and **(b)**, respectively. From **Fig.11** and **Fig.12** it can be seen that thermal analysis results are in excellent agreement with experimental results. The cooling rates, peak temperatures and final temperatures of the simulations are all agree very well with experimental results. The accurate computational results of the temperature field are a critical correlation in order to obtain accurate welding distortions.

For case 5 and case 6, the lower cooling rates and steeper thermal gradients of SUS304 stainless steel than SS400 carbon steel under the same welding heat input occur because thermal conductivity and specific heat of SUS304 stainless steel are lower than SS400 carbon steel.

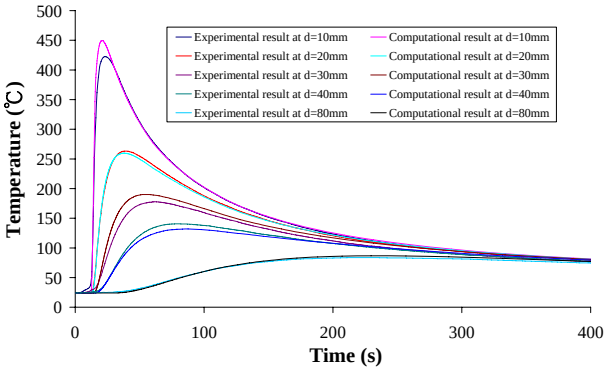

(a) Case 1

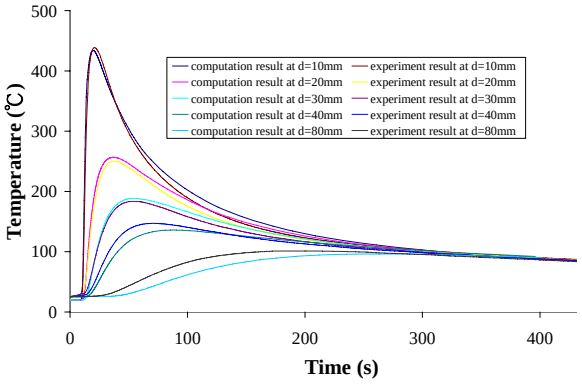

(b) Case 2

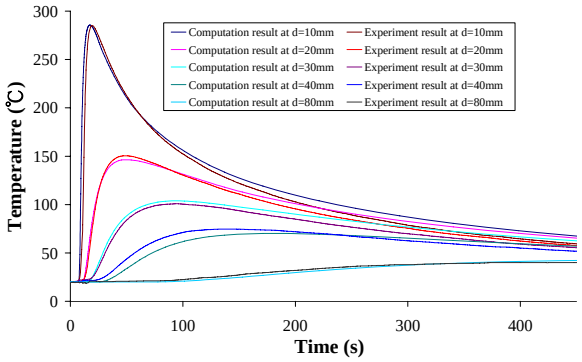

(c) Case 3

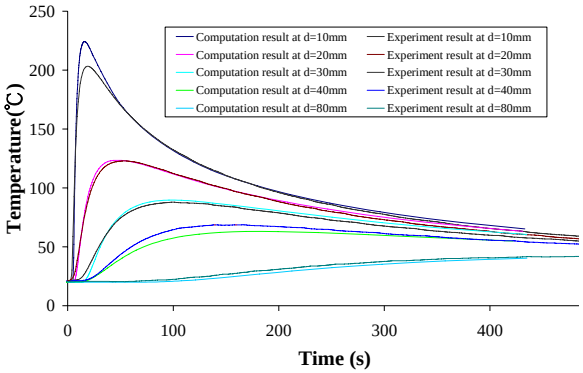

(d) Case 4

Fig.11 Temperature histories of bead on plate welding

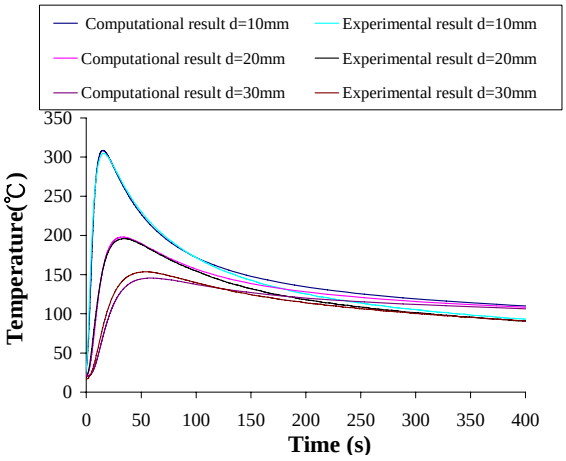

(a) Case 5

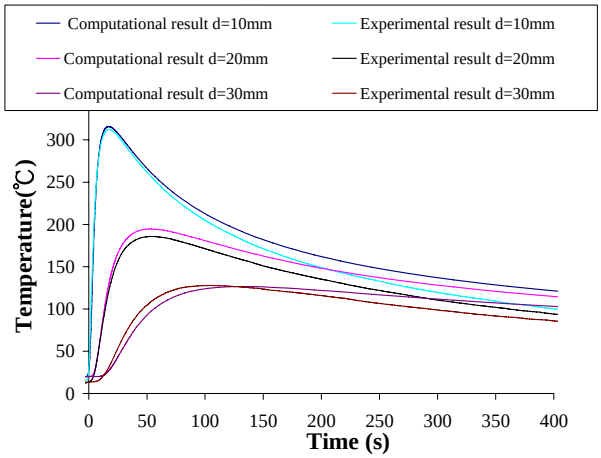

(b) Case 6

Fig.12 Temperature histories of fillet welding for the second pass

4.2 Macrosection of welding joints

The comparison of the experimental and predicted fusion boundaries for SUS304 stainless steel and SS400 carbon steel of bead on plate welding and fillet welding are given in **Fig.13** and **Fig.14**, respectively. The predictions are based on the optimum conditions such as arc efficiency, heat source power, and heat losses in the experiments. The predictions capture the overall dimensions of the fusion boundaries. From these figures it can be concluded that the overall macrosection shapes of computational and experimental results are identical. Further, the comparison results validate the effectiveness of thermal analysis.

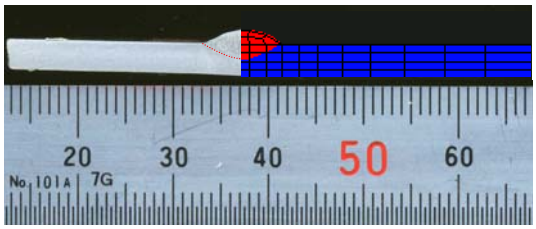

(a) Case 1

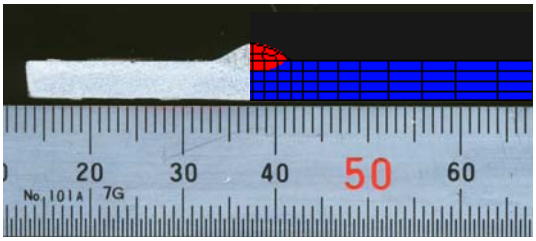

(b) Case 2

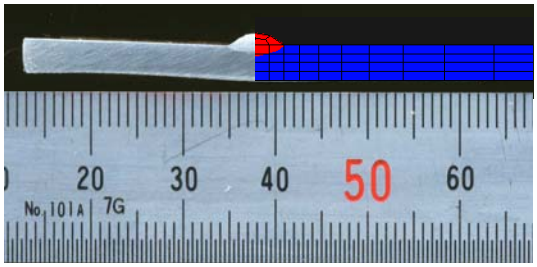

(c) Case 3

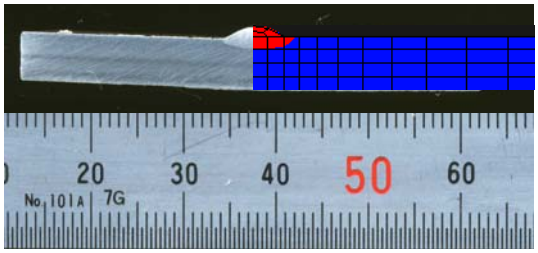

(d) Case 4

Fig.13 Macrosection of bead on plate welding

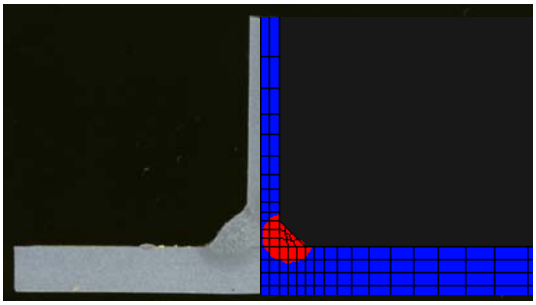

(a) Case 5

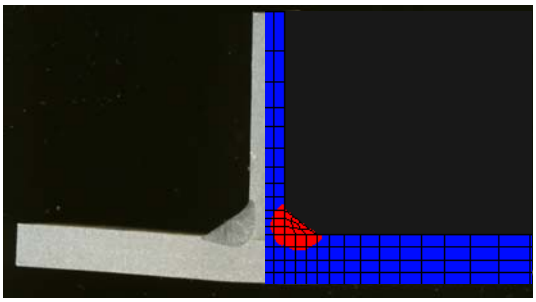

(b) Case 6

Fig.14 Macrosection of fillet welding

4.3 Welding distortions

The FE results are produced in time steps that are decided by welding time in the experiments. The main distortions to be compared in this study are the transverse shrinkage, the angular distortion, and the longitudinal shrinkage. In order to compare the results of computation and experiment, the FE results are extracted from the measurement points which were used in experiments as shown in **Figs.5-7**.

4.3.1 Transverse shrinkage

The transverse shrinkage is compared with experimental results at every measurement point after welding. **Figs.15 (a)-(f)** show the comparison of the predicted results with the experimental results of transverse shrinkage for bead on plate welding and fillet welding, respectively. The experimental and computational results of transverse shrinkage are in excellent agreement with regard to surface and bottom for bead on plate welding and fillet welding. From **Figs.15 (a)-(d)**, it can be observed that transverse shrinkage of the plate centre is larger than the two sides for bead on plate welding. This means that a bending shrinkage is produced after welding, and the plates show a little camber bending along the welding direction. **Figs.15 (e)-(f)** show the comparison of the predicted results with the experimental results of transverse shrinkage for fillet welding. These results show that the transverse shrinkage of fillet welding is different from that of bead on plate welding. The transverse shrinkage is reducing along the welding direction. The difference of transverse shrinkage between start side and end side indicates that a small twisting of the flange happened during fillet welding.

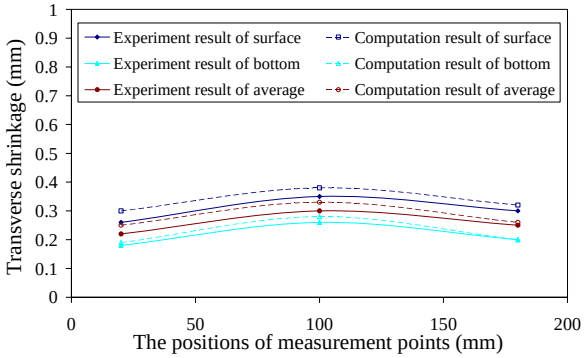

(a) Case 1

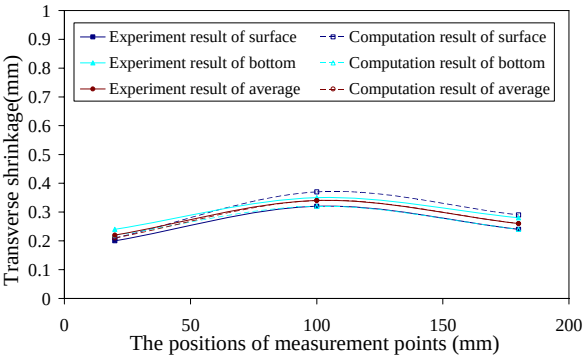

(b) Case 2

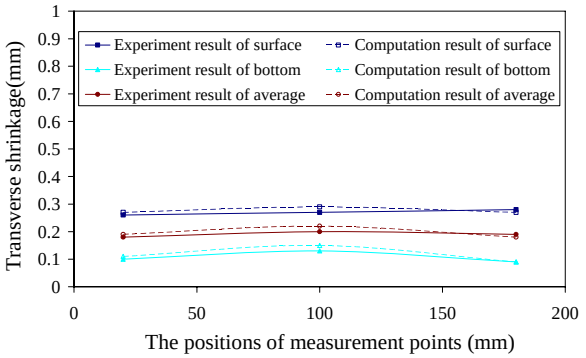

(c) Case 3

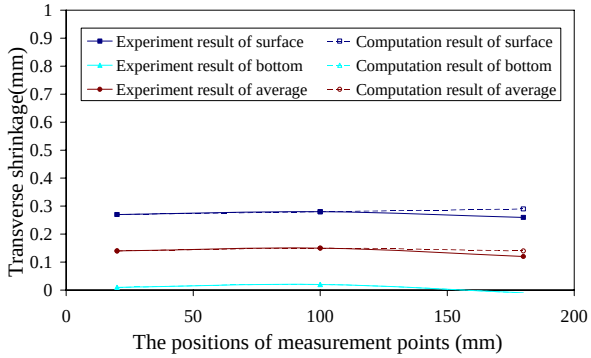

(d) Case 4

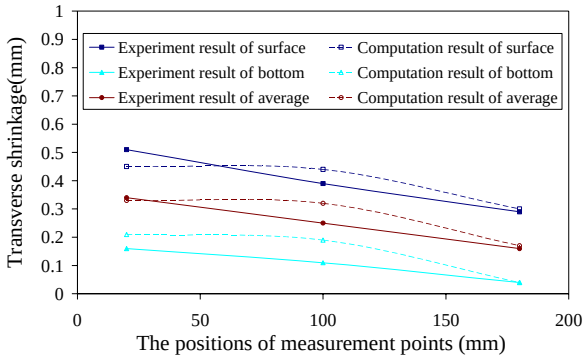

(e) Case 5

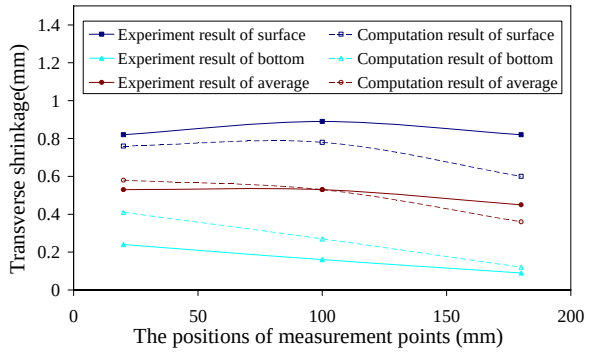

(f) Case 6

Fig.15 Transverse shrinkage

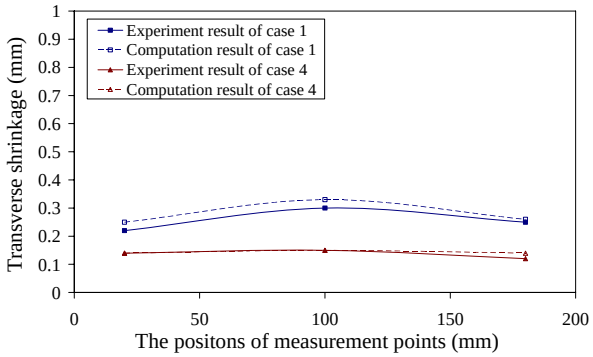

(a) Bead on plate welding

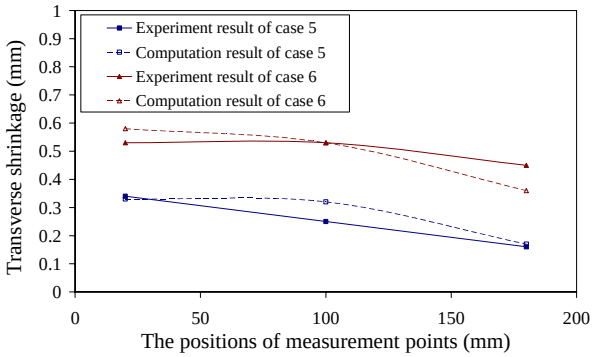

(b) Fillet welding

Fig.16 The comparison of transverse shrinkage between SUS304 stainless steel and SS400 carbon steel

Fig.16 shows the comparison of transverse shrinkage between SUS304 stainless steel and SS400 carbon steel. In order to learn about the difference of transverse shrinkage between SUS304 stainless steel and SS400 carbon steel, the average values of distortion between surface and bottom based on four cases (case 1, case 4, case 5, and case 6) are selected. **Fig.16 (a)** shows the transverse shrinkage of case 1 is larger than case 4. Transverse shrinkages both stainless steel and carbon steel increase with welding heat input increasing [15]. The welding heat input (Q/h^2) for case 1 and case 4 is 28.1 and 6.5 (J/mm^3), respectively. Compared with the welding heat input, the effect of material properties is small. So the transverse shrinkage case 1 is larger than case 4. **Fig.16 (b)** shows that the transverse shrinkage of case 6 is larger than case 5. For case 5 and case 6, the welding heat input is 34.35 and 34.07 (J/mm^3), respectively. Under the same welding condition, the effect of material properties becomes more important. As shown in **Fig.10**, the yield stress and Young's Modulus of SUS304 stainless steel is smaller than SS400 carbon steel and the thermal expansion coefficient of SUS304 stainless steel is larger than SS400 carbon steel. The smaller yield stress and Young's Modulus and larger thermal expansion coefficient plays an important role in explaining why case 6 distorts more than case 5.

4.3.2 Angular distortion

Figs.17 (a)-(f) show the comparison results of angular distortion between experiment and computation. Most of graphs among these 6 computation cases show that the magnitudes of angular distortion and the trends in each are in good agreement with experiment results. The discrepancies are produced between computation and experiment in case 2 and case 6. During the distortions simulation, for all computation cases, the influencing parameters of distortions are incorporated into the program. So, the discrepancies between experimental and computational results in case 2 and case 6 are mainly due to the measurement error and/or mesh dimension accuracy of the computational model. However, most of the results among these computational cases coincide with experimental results.

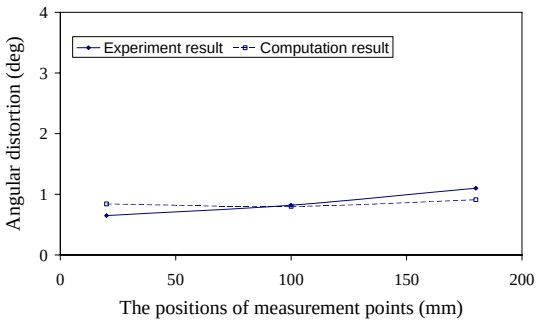

(a) Case 1

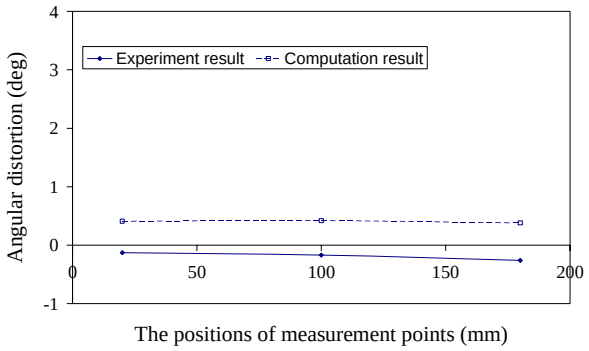

(b) Case 2

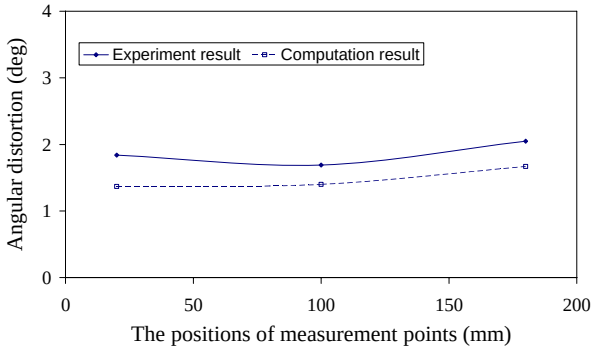

(c) Case 3

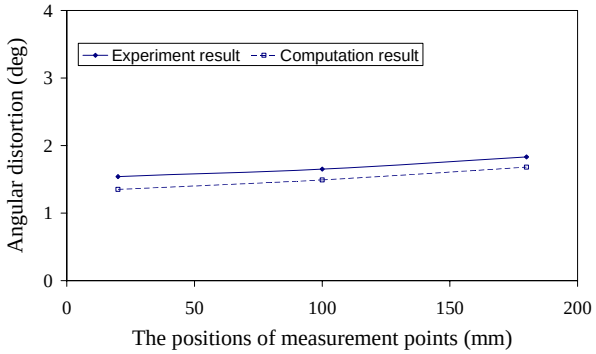

(d) Case 4

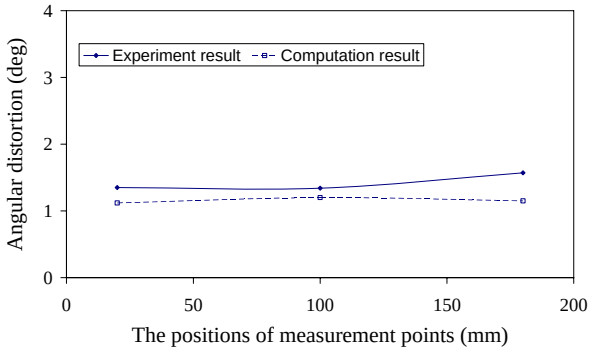

(e) Case 5

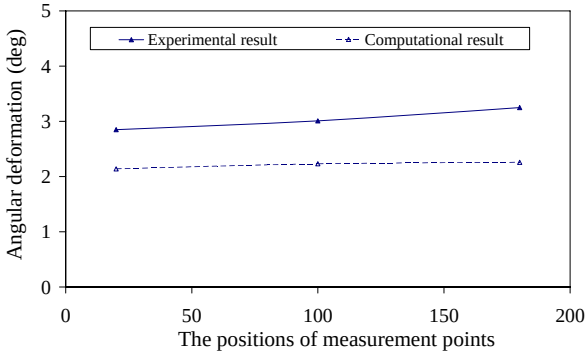

(f) Case 6

Fig.17 Angular distortion

The comparison of angular distortion between SUS304 stainless steel and SS400 carbon steel are shown in **Fig.18**. It can be observed from **Fig.18 (a)** that angular distortion of case 4 is larger than case 1. The angular distortion of case 6 is larger than case 5. Angular distortions increase with welding heat input increasing when welding heat input is lower than 10 (J/mm^3). When the welding heat input is larger than 10 (J/mm^3), the angular distortions decrease with welding heat input increasing [15]. For case 4, the welding heat input is smaller than 10 (J/mm^3) and angular distortion increases with welding heat input. While for case 1, the welding heat input is larger than 10 (J/mm^3) and angular distortion decreases with welding heat input. These computation results coincide to what might be expected from Satoh's results. The expected angular distortion results also happened in fillet welding of case 5 and case 6. Under the same welding condition, the material properties of SUS304 stainless steel and SS400 carbon steel play an important role on angular distortion.

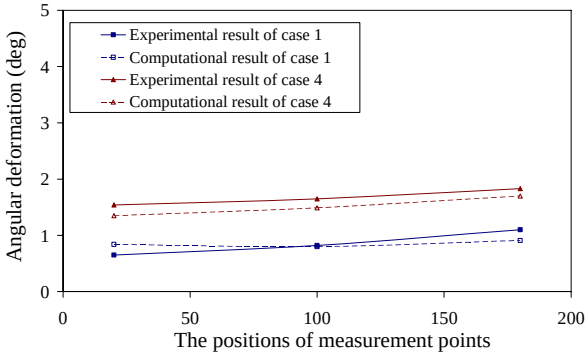

(a) Bead on plate welding

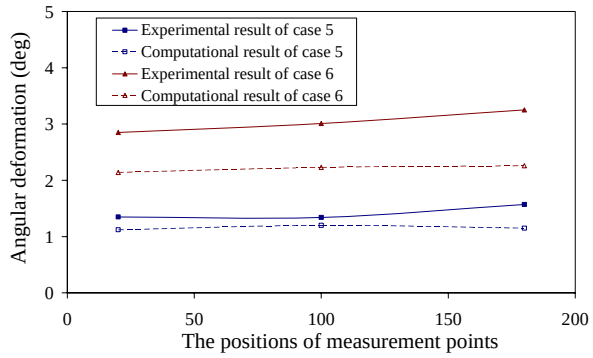

(b) Fillet welding

Fig.18 The comparison of angular distortion between SUS304 stainless steel and SS400 carbon steel

For the simulation of welding distortions on thin plate, it is necessary to consider geometrically nonlinear phenomenon [11]. **Fig.19** shows the computational results of distribution contours in the Z direction using large distortion theory and small distortion theory. **Fig.19 (a)** and **(b)** show the contour results in Z direction computed by the large distortion theory. From these two figures, it can be clearly observed that a camber bending distortion is produced after welding. The maximum deflection occurs in the middle of the plate. **Fig.19 (c)** and **(d)** show the contour results in Z direction computed by small distortion theory. Comparing with **Fig.19 (a)** and **(b)**, it can be observed that the predicted results using small distortion theory are not similar to those predicted by large distortion theory. The contrary bending distortions are predicted by the computation using small distortion theory. Moreover, the magnitudes of vertical displacements are much smaller than these computed by large distortion theory. According to the comparison results between large distortion theory and small distortion theory, it can be concluded that the distortion results computed by large distortion theory are much closer to the experimental results on thin plate welding. The large distortion theory is necessary to predict the welding distortion on thin plate welding.

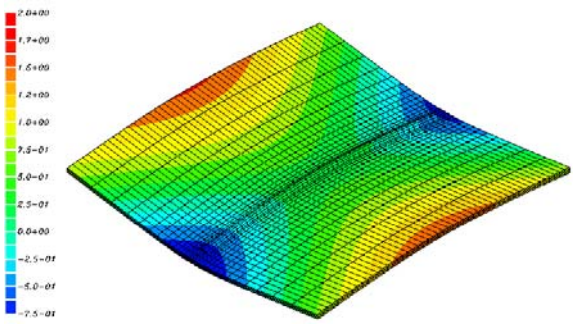

(a) Case 1 by large distortion theory

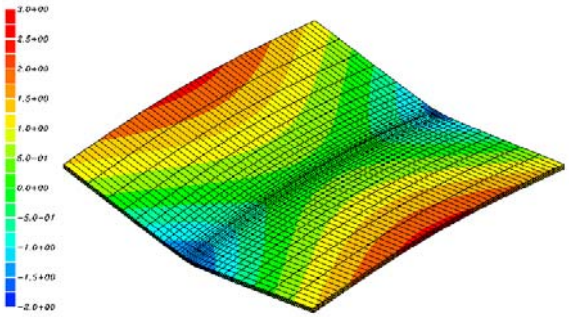

(b) Case 3 by large distortion theory

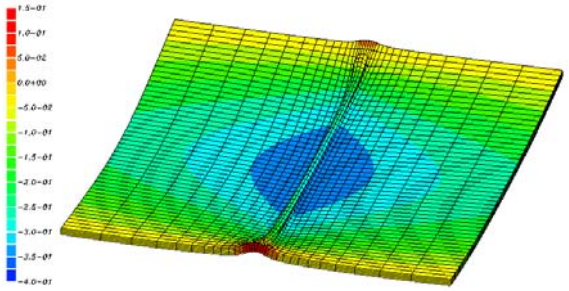

(c) Case 1 by small distortion theory

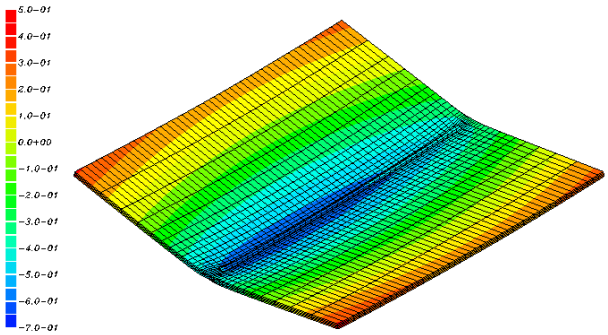

(d) Case 3 by small distortion theory

Fig.19 Contours of vertical displacement of bead on plate welding

4.3.3 Longitudinal shrinkage

The longitudinal shrinkage is caused by the longitudinal upsetting during welding resulting in a longitudinal shortening of the specimen. **Fig.20** shows the comparison of computational and experimental results of longitudinal shrinkage. From these comparison results, it can be observed that the computation results of longitudinal shrinkage are in excellent agreement with measurement results. The FE model has successfully predicted the longitudinal shrinkage of surface and bottom in bead on plate welding and fillet welding. The computation results show that longitudinal shrinkage near the weld centre is larger than at the two sides of welding specimens. This information means that the longitudinal shrinkage is notably happening in the weld zone. There is little longitudinal shrinkage produced far away from weld bead.

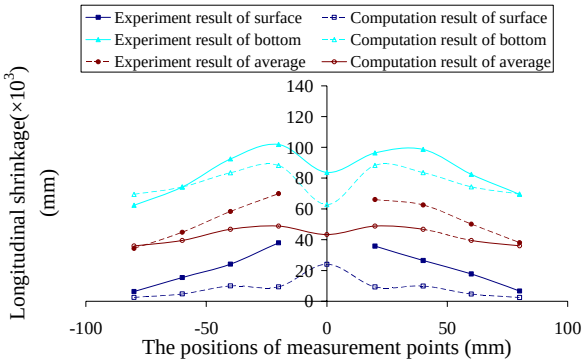

(a) Case 1

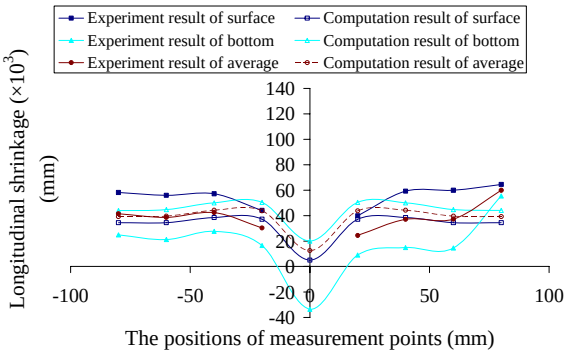

(b) Case 2

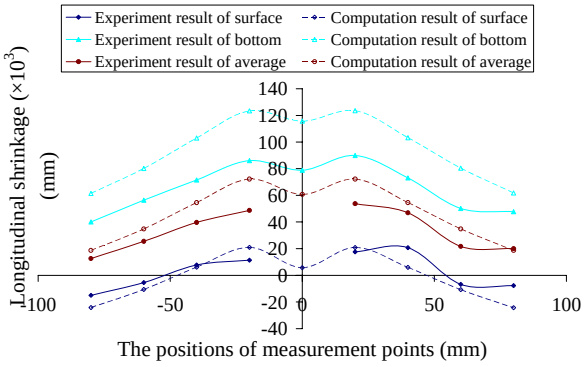

(c) Case 3

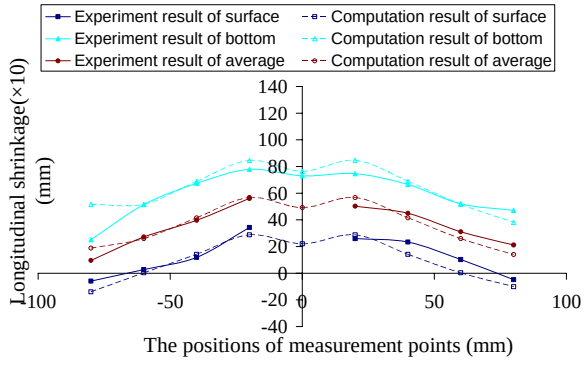

(d) Case 4

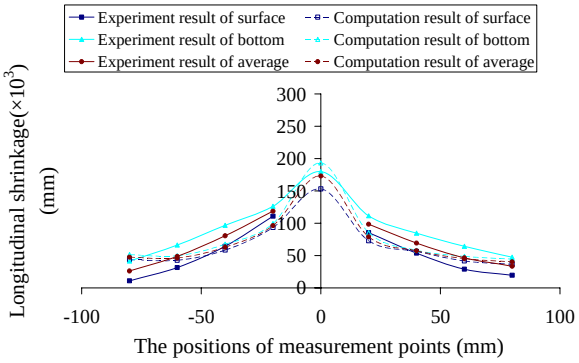

(e) Case 5

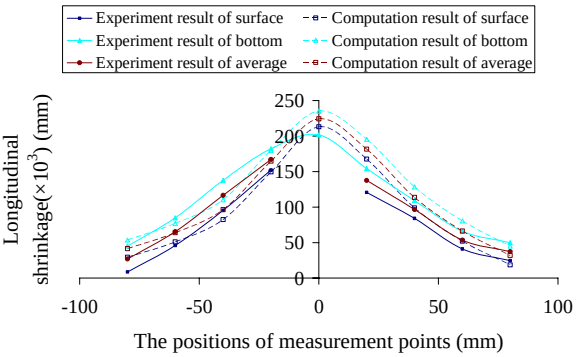

(f) Case 6

Fig.20 Longitudinal shrinkage

The longitudinal shrinkage in both stainless steel and carbon steel increases with welding heat input increasing [16]. The comparison of longitudinal shrinkage between SUS304 stainless steel and SS400 carbon steel are shown in **Fig.21 (a)** and **(b)**. The research results in this study coincide with the research results of paper [16] for longitudinal shrinkage of case 1 and case 4. The longitudinal shrinkage of case 1 is larger than case 4. The differences of material properties for SUS304 stainless steel and SS400 carbon steel are the main factors affecting the magnitude and trends of longitudinal shrinkage for the results of case 6 and case 5.

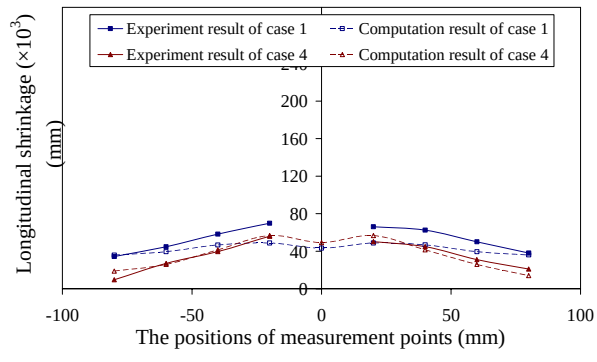

(a) Bead on plate welding

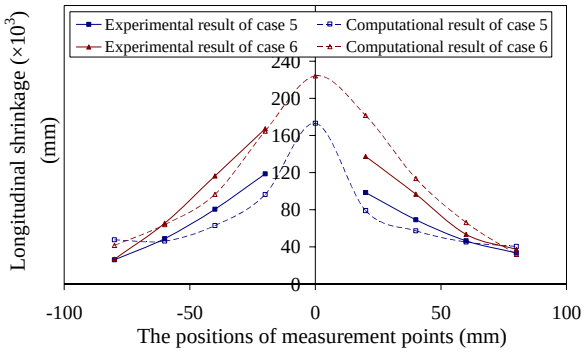

Fig.21 The comparison of longitudinal shrinkage between SUS304 stainless steel and SS400 carbon steel

5 Conclusions

In this study, the welding process of bead on plate welding and fillet welding with SUS304 stainless steel and SS400 carbon steel were investigated by ISM. Meanwhile, experiments of welding temperature history, macrosection shapes and welding distortions were made to verify the computation results.

The results show that the optimum welding process of SUS304 stainless steel and SS400 carbon steel including the welding temperature field, welding macrosection shape and welding distortions can be precisely predicted by ISM. The predicted results are in excellent agreement with experimental results. In particular, the magnitudes and trends of the transverse shrinkage, angular distortion, and longitudinal shrinkage on the surface and bottom are all successfully predicted. The results give cause for confidence in the FE simulation.

For SUS304 stainless steel and SS400 carbon steel, when the difference of welding heat input is large, the welding heat input plays an important role in welding distortion. While, material properties play a larger role in welding distortion when welding heat input is the same. In the same welding condition, the distortion of SUS304 stainless steel is larger than SS400 carbon steel. Through the comparison with experimental results, it can also be concluded that the computational results of welding distortion in thin plate welding by large distortion theory is more precise than that computed by small distortion theory. Therefore, it is necessary to incorporate the large distortion theory into the computation for the simulation of welding distortion on thin plate.

Acknowledgements

This research was the results of “Survey and research on building welding inherent deformation database and data generation”, which was supported by the New Energy and Industrial Technology Development Organization (NEDO).

References

1) P. Michaleris, A. DeBiccari. Weld. J. 76 (4): 172–18, 1997.
2) M.V. Deo, P. Michaleris, J. Sun. Sci. Technol. Weld. Join. 8 (1): 55–61, 2003.
3) D.Camilleri, T. Comlekci, T.G.F.Gray. J. Strain. Anal. 40 (2): 161-176, 2005.
4) C.L. Tsai, S.C. Park, W.T. Cheng. Weld. J. 78 (5): 157–165, 1999.
5) H.Murakawa. Mater. Sci. Forum. 539-543: 181-186, 2007.
6) H.Nishikawa, H.Serizawa, H.Murakawa. Sci. Technol. Weld. Join. 12(2): 147-152, 2007.
7) W.Liang, S.J. Sone, M. Tejima, H. Serizawa, H.Murakawa. Transactions of JWRI. 33(1): 45-51, 2004.
8) W.Liang, D.A. Deng, H.Murakawa. Transactions of JWRI. 34(1): 113-123, 2005.
9) D. A. Deng, H. Murakawa, W. Liang. Comput. Methods Appl. Mech. Engrg. 196: 4613-4627, 2007.
10) D. A. Deng, W. Liang, H. Murakawa. J. Mater. Process. Tech. 183: 219-225, 2007.
11) D. A. Deng, H. Murakawa. Comp. Mater. Sci. 2008 (In press)
12) J.M.J.McDill, A.S.Oddy, J.A.Goldak, S.Bennison. J. Strain. Anal. 25(1): 51-53, 1990.
13) H.Nishikawa, I.Oda, M.Shibahara, H.Serizawa, H.Murakawa. Proc.Int.Soc.Offshore Polar Eng. Conf., Toulon, France. May 2004, ISOPE, 126-132.
14) H.Nishikawa, I.Oda, H.Serizawa, H.Murakawa. Transactions of JWRI. 33(2): 161-166, 2004.
15) K. Satoh, T. Terasaki. Quar. J. JWS. 45(4): 302-308, 1976. (In Japanese)
16) T.Terasaki, T.Ishimura, K.Matsuishi, T.Akiyama. Quar. J. JWS. 20(1): 136-142, 2002. (In Japanese).